

# Triple-decker: Interfacing atomistic–mesoscopic–continuum flow regimes

Dmitry A. Fedosov, George Em Karniadakis\*

Division of Applied Mathematics, Brown University, 182 George St., Box F, Providence, RI 02912, USA

## ARTICLE INFO

### Article history:

Received 29 January 2008

Received in revised form 23 September 2008

Accepted 12 October 2008

Available online 29 October 2008

### Keywords:

Multiscale simulation

Hybrid methods

MD

DPD

Navier–Stokes

## ABSTRACT

Multiscale flow phenomena in microfluidic and biomedical applications require the use of heterogeneous modeling approaches. In this paper we present a hybrid method based on coupling the Molecular Dynamics (MD) method, the Dissipative Particle Dynamics (DPD) method, and the incompressible Navier–Stokes (NS) equations. MD, DPD, and NS are formulated in separate subdomains and are coupled via an overlapping region by communicating state information at the subdomain boundaries. Imposition of boundary conditions in the MD and DPD systems involves particle insertion and deletion, specular wall reflection and body force terms. The latter includes a boundary pressure force in order to minimize near-boundary density fluctuations, and an *adaptive* shear force which enforces the tangential velocity component of boundary conditions. The triple-decker algorithm is verified for prototype flows, including simple and multi-layer fluids (Couette, Poiseuille, and lid-driven cavity), using highly accurate reference solutions. A zero-thickness interface is also possible if it is aligned with the flow streamlines.

© 2008 Elsevier Inc. All rights reserved.

## 1. Introduction

In many microfluidic and biomedical applications there is often a need to model accurately multiscale flow phenomena across several orders of magnitude in spatiotemporal scales. Examples in the first category include flow over nanotubes with hydrophobic surfaces and electroosmotic flows [1], where flow phenomena within a layer of less than 10 nm from the wall may have a profound effect on the global dynamics. Examples in the second category include cytoadhesion [2] and platelet aggregation [3], where interactions of freely flowing cells with protein-coated walls govern the overall dynamics. In both cases it is important to capture *molecular details* within a near-wall subdomain but also resolve *efficiently* the outer flow. To this end, molecular dynamics (MD) simulations can be employed to resolve the near-wall structure but cannot be used in big domains due to its unfavorable computational scaling compared to continuum discretizations. Multiscale approaches both in time and space can overcome this difficulty and provide a unified description of liquid flows from nanoscales to larger scales. The majority of existing multiscale methods [4–10] attempt to “glue” together atomistic and continuum approaches corresponding to MD and Navier–Stokes (NS), respectively. However, between atomistic and continuum scales lies an intermediate range called *mesoscopic*, which exhibits features of both the atomistic and continuum descriptions. Over the last decade, there has been great progress in developing efficient numerical methods for this regime; the most popular method is the Lattice Boltzmann method (LBM) [11], but other Lagrangian-type methods have also emerged, e.g. the Dissipative Particle Dynamics (DPD) [12,13] and the Smoothed Particle Hydrodynamics (SPH) [14,15]. Remarkably, the mesoscopic level is simply omitted in the atomistic/continuum paradigm although a few attempts have been made recently to couple atomistic and mesoscopic descriptions directly, specifically MD and LBM [16,17]. However, to the best of our knowledge, there is no published hybrid

\* Corresponding author. Tel.: +1 401 863 1217; fax: +1 401 863 3369.

E-mail address: [gk@dam.brown.edu](mailto:gk@dam.brown.edu) (G.E. Karniadakis).

atomistic–mesoscopic–continuum method for multiscale flow phenomena, which would combine the advantages of all three levels of description.

There are two main coupling approaches:

- (1) The *flux-exchange* method [4–7] is based on the flux-exchange between continuum and particle domains.
- (2) The *state-exchange* method [8–10,16,17] is based on the alternating Schwarz method [18].

More specifically, the flux-exchange method is based on the direct exchange of flux information in the overlap domain between the particle region and the continuum region, and relies on the matching of fluxes of mass, momentum and energy. In the state-exchange method the state information between the particle simulation and the NS equations is transferred through an overlap region where the particles's dynamics is constrained; the constrained dynamics is often imposed via a dynamic relaxation technique [10]. The alternating Schwarz method is used to solve sequentially the problems in the continuum and atomistic domains, and state-exchange is performed until convergence is achieved. The main difficulty here is extraction and imposition of the required state information in particle-based methods. The extraction of the mean flowfield properties requires sampling of flow characteristics over some region and often over a time interval. This fact makes the application of the flux-exchange model difficult and favors the alternating Schwarz method. However, the Schwarz method appears to be more restrictive in the case of dynamic simulations of unsteady flows.

The choice of a particular multiscale algorithm depends strongly on the flow problem. Several algorithm characteristics (e.g. performance, applicability and robustness) may be considered. The main requirement for all available algorithms is conservation of mass, momentum and energy. For instance, conservation of momentum and energy in particle-based methods is often imposed on average and is not satisfied at every fixed point of time. The applicability of a particular algorithm may be restricted, for example, to steady flows as well as to a certain range of flow regimes. The algorithm robustness includes the ability of the hybrid method to efficiently decouple length and time scales. Both of the aforementioned coupling approaches lead to a reasonably good decoupling of spatial scales. However, the state-exchange method enables less restrictive temporal coupling than the flux-exchange method. In this work we employ the state-exchange method for coupling atomistic, mesoscopic, and continuum formulations.

The paper is organized as follows: in Section 2 we describe the coupling among regions with different formulations. Details of atomistic modeling are presented in Section 2.1, mesoscopic modeling in Section 2.2, and continuum modeling in Section 2.3. Simulation results of the triple-decker algorithm for Couette, Poiseuille and lid-driven cavity flows are presented in Section 3. We conclude in Section 4 with a brief discussion.

## 2. Triple-decker algorithm

In this section we describe the coupling mechanism. The hybrid coupling technique used in this paper is based on the domain decomposition similar to the Schwarz alternating method [18]. The flow domain is decomposed into three (or potentially more) overlapping regions: an atomistic region described by MD, a mesoscopic region described by DPD, and a continuum region represented by spectral element discretization of the incompressible NS equations.

A schematic of the domain decomposition (left) and the time progression (right) is shown in Fig. 1. Each subdomain is subject to Dirichlet velocity boundary conditions (BCs). The integration in each region is performed independently, and coupling among different subdomains is done through BC communications. As an example, in Fig. 1 BCs for the DPD region will be provided from both MD and NS regions, and in turn, BCs for the MD and NS subdomains will be extracted from the DPD region. The communication with necessary BCs information among subdomains is done every  $\tau$  in time progression as shown in Fig. 1. Note that the time  $\tau$  between two successive communications may correspond to a different number of time

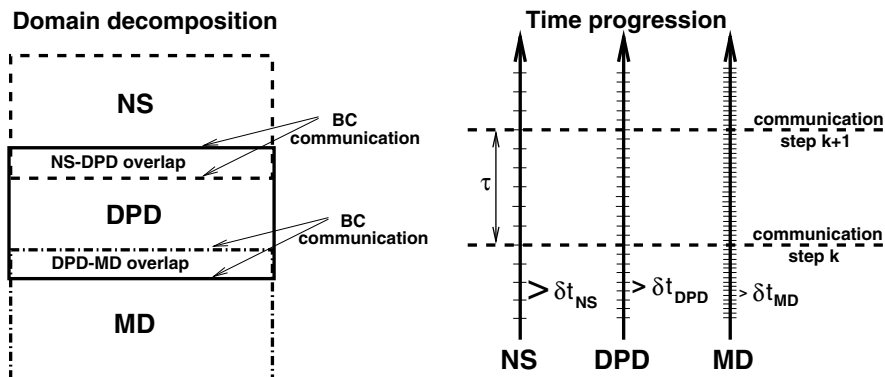


Fig. 1. A schematic of the MD-DPD-NS domain decomposition (left) and the time progression (right).

steps for the three descriptions. For instance, Fig. 1 shows the smallest timestep  $\delta t_{\text{MD}}$  chosen for the MD simulation, a larger  $\delta t_{\text{DPD}}$  for DPD, and the largest time step  $\delta t_{\text{NS}}$  for the Navier–Stokes formulation, which illustrates an effective temporal decoupling. In addition, the time interval  $\tau$  can be manually set and potentially changed during simulation depending on the flow development, i.e. prescribe small  $\tau$  for transient flow and larger  $\tau$  for steady state. There are many possible communication patterns which can be used for the simulation progressing in time. For instance, one could run all the subdomains simultaneously and carry out BCs communications every  $\tau$ . Another option is to run the subdomains sequentially in the chosen order, such that one subdomain is advanced during  $\tau$ , BCs are passed to the second subdomain, and in turn the second subregion is integrated during  $\tau$ , and so forth. The algorithm allows one to freely select subdomain dimensions (e.g. length and width), timestep for integration and, if needed, fluid properties (e.g. viscosity for multi-layer fluid), because the subdomains are integrated separately and are coupled only through BCs.

An extraction of BCs from particle subdomains such as MD and DPD involves *velocity averaging*. A number of cells is present along the line of interest, where the local velocity field is sampled, and the averaging is carried out during a number of timesteps. However, one has to be aware of the associated statistical error  $E_v$ , which depends on the number of samples  $M_v$ , the corresponding cell average  $\bar{v}$  and standard deviation  $\sigma(v)$  of desired flow properties. Hadjiconstantinou et al. [19] obtained an *a priori* estimate for the number of samples  $M_v$  required to measure the average of velocities in a cell of volume  $V$  for fixed error  $E_v$ , as follows:

$$M_v = \frac{k_B T}{\bar{v}^2} \frac{1}{\rho V E_v^2}, \quad (1)$$

where  $\bar{\rho}$ ,  $T$  and  $k_B$  are the average density, temperature and Boltzmann constant, respectively. Note that one sample ( $M_v = 1$ ) corresponds to the averaging over  $\bar{n}V = \frac{\rho}{m}V$  particle velocities or over all particles in volume  $V$  during a single timestep, where  $\bar{n}$  is the average number density and  $m$  is the particle mass. This formula provides the correct estimate assuming that the samples are statistically independent, which is generally not valid for MD and DPD fluids if sampling is performed every timestep. If the samples are correlated, the number of samples required to estimate the average of velocity is equal to

$$M_v^c = 2 \frac{\tau_v}{\delta t} M_v, \quad (2)$$

where  $\tau_v$  is the autocorrelation time [20]. The autocorrelation time is proportional to the fluid self-diffusion coefficient  $D$  because of the Green–Kubo relation:  $D = \frac{1}{3} \int_0^\infty A_v(t) dt$ , where  $A_v(t)$  is the velocity autocorrelation function defined as  $A_v(t) = Ce^{-t/\tau_v}$ , where  $C$  is a constant. We have used the above equations in order to determine the number of samples required to keep the error  $E_v$  below 5%, see Section 3.

## 2.1. Atomistic region via molecular dynamics

The atomistic region is necessary in flow parts where the continuum formalism breaks down or where atomistic level physics needs to be captured. We model the atomistic subdomain using MD, but in combination with the DPD thermostat [12,13]. Next, we describe the MD method and the imposition of BCs.

### 2.1.1. MD governing equations with DPD thermostat

The molecular dynamics system consists of  $N$  point particles of mass  $m_i$ , position  $\mathbf{r}_i$  and velocity  $\mathbf{v}_i$ . The particles evolve according to Newton's second law of motion

$$d\mathbf{r}_i = \mathbf{v}_i dt, \quad (3a)$$

$$d\mathbf{v}_i = \frac{1}{m_i} \sum_{j \neq i} (\mathbf{F}_{ij}^U dt + \mathbf{F}_{ij}^D dt + \mathbf{F}_{ij}^R \sqrt{dt}), \quad (3b)$$

where  $\mathbf{F}_{ij}^U = \nabla U(r_{ij})$  are Lennard–Jones interparticle forces and  $\mathbf{r}_{ij} = \mathbf{r}_i - \mathbf{r}_j$ ,  $r_{ij} = |\mathbf{r}_{ij}|$ .  $\mathbf{F}_{ij}^D$  and  $\mathbf{F}_{ij}^R$  are dissipative and random forces, which define the DPD thermostat described in the DPD method, see Section 2.2. Soddemann et al. [21] showed that it is advantageous to use the DPD thermostat in MD as it is completely local and allows *longer timesteps* compared to conventional thermostats without sacrificing accuracy. The Lennard–Jones potential is given by

$$U(r_{ij}) = 4\epsilon \left[ \left( \frac{\sigma_{\text{MD}}}{r_{ij}} \right)^{12} - \left( \frac{\sigma_{\text{MD}}}{r_{ij}} \right)^6 \right], \quad (4)$$

where  $\epsilon$  and  $\sigma_{\text{MD}}$  are energy and length characteristic parameters, respectively. All interactions vanish beyond a *cutoff radius*  $r_c$ . The equations of motion were integrated using the modified velocity-Verlet algorithm [13].

### 2.1.2. MD for non-periodic systems

Here we describe a model which imposes non-periodic BCs in MD. Two main issues are considered: (i) correct imposition of local velocity at the boundary and (ii) control of local disturbance effect on density, pressure and temperature.

The first problem is subdivided into imposition of the normal  $v_n$  and the tangential  $v_t$  components of velocity. The tangential component of velocity at the boundary is enforced through an *adaptive shear force*: each particle with distance  $h < r_c$  from the boundary is subject to a tangential force  $F_t^k(h)$  depending on the distance  $h$ . The force is defined as

$$F_t^k(h) = C_k(\Delta v_t)w(h), \quad (5)$$

where  $k$  is the iteration number,  $C_k(\Delta v_t)$  is an adaptive force *strength* and  $w(h)$  is a *weight function* defined as  $w(h) = \left(1 - \frac{h}{r_c}\right)^4$ . The adaptive force strength is calculated iteratively as  $C_{k+1} = C_k + \alpha \Delta v_t$ , where  $\alpha$  is a *relaxation parameter* which can be set to a constant value similar to [4] or calculated adaptively as proposed in [10]. In this work we set the relaxation parameter to  $\alpha = 1.0$ , but future work will incorporate a dynamic approach. Here, we define  $\Delta v_t = v_t^{\text{BC}} - v_t^{\text{est}}$  with  $v_t^{\text{BC}}$  the assigned velocity at the boundary and  $v_t^{\text{est}}$  an estimated flow velocity at the boundary. The near-boundary velocity profile is estimated by local cell averaging of particle velocities during every  $m$  timesteps. Next,  $v_t^{\text{est}}$  is calculated by extrapolation from the estimated near-boundary velocity profile, and recalculation of the adaptive shear force is performed. Here, we employ a first-order extrapolation based on two points in the near-boundary region. In general, higher order extrapolation can be implemented, however it requires estimation of larger number of points in the near-boundary velocity profile. After a number of iterations, we find that  $\Delta v_t \approx 0$ , so that  $C_k$  and  $F_t^k(h)$  converge to a constant value, which leads to the proper tangential BC velocity  $v_t = v_t^{\text{BC}}$ .

Imposition of the normal velocity component  $v_n$  is carried out by *particle insertions and reflections* similarly to [9]. In order to satisfy total mass conservation we need to keep the total number of particles in the system constant. Particles that strike the boundary are *specularly* reflected in a frame of reference attached to the moving boundary. The collision time is calculated as  $t' = (x^k - x_{\text{BC}})/(v_{\text{BC}} - v^k)$ , where  $x_{\text{BC}}$  and  $v_{\text{BC}}$  are the boundary position and the boundary speed, and  $x^k$  and  $v^k$  are the position and the normal velocity of a particle. If a particle crosses the boundary ( $0 \leq t' \leq \delta t_{\text{MD}}$ ) during one timestep, a new particle velocity and position are computed according to the following equations:

$$v^{k+1} = 2v_{\text{BC}} - v^k, \quad (6a)$$

$$x^{k+1} = x^k + t'v^k + (\delta t_{\text{MD}} - t')v^{k+1}. \quad (6b)$$

Note that only the normal to the boundary component is updated, while the two tangential to the boundary components (in 3D) remain unchanged. After particle reflection is completed, the average number of particles that have left the domain is equal to the particle flux through the boundary  $n\delta t_{\text{MD}}Av_n$ , where  $n$  is the number density and  $A$  is the area. Particles that have left the domain are re-inserted into near boundary layer according to the probability associated with the particle flux through the boundary using the *USHER* algorithm [22]. The *USHER* algorithm provides numerical stability of the insertion procedure and minimizes local disturbances in fluid properties. Inserted particle velocities are drawn from a Maxwellian distribution according to the local boundary velocity. In addition, we added an *adaptive normal force* of similar type as in Eq. (5). However, we found that the insertion and reflection of particles appears to be sufficient to enforce a correct normal velocity at the boundary, so the adaptive normal force was turned off in most of our calculations. Note that insertion and reflection of particles does not conserve instantaneous momentum, however the total system momentum is conserved *on average*.

We now address the second issue of minimizing local disturbances in fluid properties. As we mentioned before, the *USHER* algorithm works well for the particle insertion. However, another problem is *erroneous* density fluctuations near the boundary, which appear due to an imbalance of forces from the surrounding fluid (a particle near the boundary interacts with a not-fully spherical region of fluid particles). In order to compensate for the force imbalance, we apply the following pressure force in the near-boundary region similarly to [9,23]:

$$F_p(h) = -n \int_{V_s \setminus V_{\text{ex}}(h)} \frac{\partial U}{\partial \mathbf{r}} g(r) dV, \quad (7)$$

where  $V_s$  is the sphere volume,  $V_{\text{ex}}(h)$  is a volume excluded from the sphere by the boundaries, and  $g(r)$  is the radial distribution function. The calculation of the above integral requires computing the radial distribution function for the specific fluid used in the simulations. Note that the pressure force  $F_p(h)$  can be also calculated directly from an equilibrium simulation for a fictitious boundary.

## 2.2. Mesoscopic region via dissipative particle dynamics

The mesoscopic region might cover the flow region where the continuum formalism is not valid while a fully atomistic simulation is not feasible due to computational cost. The mesoscopic subdomain is modeled through the DPD method described next.

### 2.2.1. DPD governing equations

DPD is a mesoscopic particle method and, unlike MD, each DPD particle represents a *molecular cluster* rather than an individual atom, and can be thought of as a soft lump of fluid. Similarly to MD, the DPD system consists of  $N$  point particles of mass  $m_i$ , position  $\mathbf{r}_i$  and velocity  $\mathbf{v}_i$ . DPD particles interact through three forces: conservative, dissipative and random forces given by

$$\mathbf{F}_{ij}^C = F_{ij}^C(r_{ij})\hat{\mathbf{r}}_{ij}, \quad (8a)$$

$$\mathbf{F}_{ij}^D = -\gamma\omega^D(r_{ij})(\mathbf{v}_{ij} \cdot \hat{\mathbf{r}}_{ij})\hat{\mathbf{r}}_{ij}, \quad (8b)$$

$$\mathbf{F}_{ij}^R = \sigma\omega^R(r_{ij})\xi_{ij}\hat{\mathbf{r}}_{ij}, \quad (8c)$$

where  $\hat{\mathbf{r}}_{ij} = \mathbf{r}_{ij}/r_{ij}$ , and  $\mathbf{v}_{ij} = \mathbf{v}_i - \mathbf{v}_j$ . The coefficients  $\gamma$  and  $\sigma$  define the strength of dissipative and random forces, respectively. In addition,  $\omega^D$  and  $\omega^R$  are weight functions, and  $\xi_{ij}$  is a normally distributed random variable with zero mean, unit variance, and  $\xi_{ij} = \xi_{ji}$ . All forces are truncated beyond the cutoff radius  $r_c$ , which defines the length scale in the DPD system. The conservative force is given by

$$F_{ij}^C(r_{ij}) = \begin{cases} a_{ij}(1 - r_{ij}/r_c) & \text{for } r_{ij} \leq r_c, \\ 0 & \text{for } r_{ij} > r_c, \end{cases} \quad (9)$$

where  $a_{ij} = \sqrt{a_i a_j}$  and  $a_i, a_j$  are conservative force coefficients for particles  $i$  and  $j$ , respectively.

The random and dissipative forces form a thermostat and must satisfy the fluctuation–dissipation theorem in order for the DPD system to maintain equilibrium temperature  $T$  [24]. This leads to:

$$\omega^D(r_{ij}) = [\omega^R(r_{ij})]^2, \quad (10a)$$

$$\sigma^2 = 2\gamma k_B T, \quad (10b)$$

where  $k_B$  is the Boltzmann constant. The choice for the weight functions is as follows

$$\omega^R(r_{ij}) = \begin{cases} (1 - r_{ij}/r_c)^k & \text{for } r_{ij} \leq r_c, \\ 0 & \text{for } r_{ij} > r_c, \end{cases} \quad (11)$$

where  $k = 1$  for the original DPD method. However, other choices (e.g.  $k = 0.25$ ) for these envelopes have been used [23,25,26] in order to increase the viscosity of the DPD fluid.

The time evolution of velocities and positions of particles is determined by Newton's second law of motion similarly to MD method, which is integrated using the modified velocity-Verlet algorithm [13].

### 2.2.2. Boundary conditions in DPD

Non-periodic boundary conditions in the DPD region are imposed analogously to the MD region. The tangential component of velocity is enforced through the adaptive shear force  $F_t^k(h)$ . Imposition of normal velocity component is performed by insertion and reflection of particles as described in Section 2.1. However, here the *USHER* algorithm is omitted. We found that the system remains stable with *random* insertions. Moreover, a disturbance to the local properties appears to be on the order of several percent which is similar to deviations introduced by the thermostat. No special algorithm is required for insertions because of soft particle interactions in DPD compared to hard MD particle interactions. In order to minimize near-boundary density fluctuations we use a similar pressure force  $F_p(h)$  as for the MD subdomain, see also [27].

### 2.3. Continuum model

The continuum part of the hybrid system is governed by the incompressible NS equations in the form

$$\frac{\partial \mathbf{u}}{\partial t} + (\mathbf{u} \cdot \nabla) \mathbf{u} = -\frac{1}{\rho} \nabla p + \nu \nabla^2 \mathbf{u}, \quad (12a)$$

$$\nabla \cdot \mathbf{u} = 0, \quad (12b)$$

where  $\mathbf{u}$  is the fluid velocity,  $\rho$  is the density,  $p$  is the pressure and  $\nu$  is the kinematic viscosity. At the boundary we specify Dirichlet velocity boundary conditions. The NS equations are solved using the spectral/hp element discretization implemented in the parallel solver NEKTAR [28].

## 3. Simulation results

We test the triple-decker algorithm for three flows: Couette, Poiseuille and lid-driven cavity flow. We compare the hybrid simulation results with an exact solution for the Couette and Poiseuille flows, and with numerical solution for the cavity flow obtained by a highly resolved spectral element discretization of the NS equations.

### 3.1. Couette and Poiseuille flows

We apply the MD–DPD–NS algorithm to the cases of Couette and Poiseuille flows. Fig. 2 shows a sketch of the domain used in both simulations. The fluid is confined between two parallel walls placed at  $y = 0$  and  $y = H = 20$  with velocities  $v_0$  and  $v_1$ , respectively. For the case of Couette flow we set  $v_0 = 0$ ,  $v_1 = 5$ , and for Poiseuille flow  $v_0 = v_1 = 0$ . Table 1 presents the parameters used in the MD and DPD regions. The domain is assumed to be periodic in  $x$  direction, and for MD and

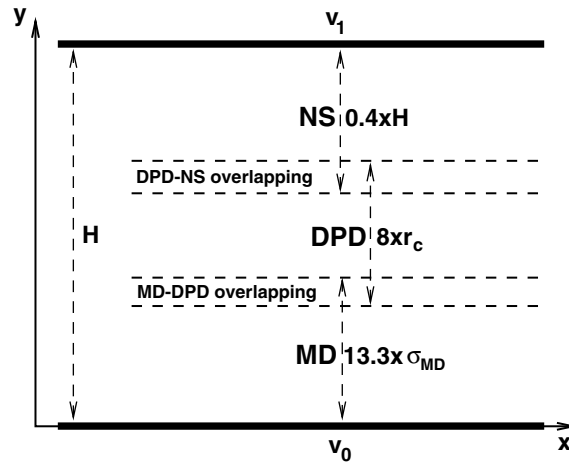


Fig. 2. Sketch for the Couette and Poiseuille flow domain.

Table 1

MD and DPD simulation parameters.

Region	$\epsilon$	$\sigma_{MD}$	$a$	$n$	$r_c$	$\gamma$	$\sigma$	$k_B T$	$k$ (Eq. (11))
MD	0.3	0.6	N/A	3	1	4.5	3	1	1.0
DPD	N/A	N/A	25	3	1	4.5	3	1	0.221

DPD also in  $z$  direction. The width of MD, DPD and NS layers was set to  $13.3 \times \sigma_{MD}$ ,  $8 \times r_c$  and  $0.4 \times H$ , respectively. The time-step in all regions was chosen to be 0.005 and the kinematic viscosity  $\nu$  was equal to 0.576 in common (for all three descriptions) non-dimensional units. The viscosity in case of MD and DPD was calculated using the periodic Poiseuille flow method of [29]. In the case of Poiseuille flow the fluid is driven by a constant pressure gradient equal to 0.03 (non-dimensional units). The overlapping regions have thickness  $\delta = 2$ . The thickness of overlap is a free parameter, however it may have a strong effect on the flow convergence. While it is desirable to have a minimal overlap due to the computational expense,  $\delta$  must be greater than zero because the overlapping region is responsible for the propagation of information among regions with different formulations. For instance, in case of the Couette flow (Fig. 2) the flow development is initiated at the upper wall and propagates downwards through the NS region. Having  $\delta = 0$  would not allow propagation of flow development in the DPD region. In addition,  $\delta \sim 0$  might provide an extremely slow flow development. Several tests we performed suggest that the overlapping region should approximately have a thickness on the order of 10% of the flow characteristic length.

The coupling process was performed every time  $\tau = 0.5$  which corresponds to 100 timesteps. The coupling time  $\tau$  was chosen according to Eqs. (1) and (2) as follows: here  $k_B T = 1$ ,  $\bar{v} = 2.5$ ,  $\bar{\rho} = 3.0$ ,  $V = 10 \times 10 \times 0.5 = 50$  and  $E_v = 0.05$  lead to  $M_v = 0.427$ , which corresponds to averaging over approximately 64 particle velocities. The autocorrelation time  $\tau_v = 0.45$  yields  $M_v^c = 77$ . Taking into account that some estimated velocities are below 2.5 we set the number of samples to 100 timesteps. One iteration of the algorithm corresponds to the flow integration during time  $\tau$  and is performed as follows: the NS solver is advanced during the time  $\tau$  and BCs are extracted and passed to the DPD subdomain. Then, DPD is advanced during  $\tau$  and BCs are passed to the MD and NS regions (see Fig. 2). Next, the MD subdomain is integrated during time  $\tau$  and BCs for the DPD region are extracted. Thus, a single iteration of the triple-decker algorithm corresponds to the sequence of region integrations NS  $\rightarrow$  DPD  $\rightarrow$  MD. The choice of the sequence is solely based on the type of flow, such that the flow development propagates from the moving wall downwards through the NS  $\rightarrow$  DPD  $\rightarrow$  MD regions to the stationary lower wall. Note that for the case of Poiseuille flow an analogous sequence MD  $\rightarrow$  DPD  $\rightarrow$  NS can be selected due to symmetry. This type of iteration is performed until the system relaxes to a steady state solution. The number of iterations required to reach steady state depend on many factors, such as flow and fluid properties (e.g. viscosity, Reynolds number and geometry), the relative geometric complexity of different domains, the overlapping regions (e.g. thickness and complexity), the BC relaxation technique, etc. Here the number of iterations to reach steady state was on the order of  $O(10^2)$ . After the steady state was reached, we carried out averaging of the flow field over  $10^5$  timesteps.

Fig. 3 presents hybrid simulation results of Couette and Poiseuille flows. We find an excellent agreement of the triple-decker method results with the exact solution. In addition, we have observed *no density fluctuations* across the channel. However, this system corresponds to a relatively simple coupling among regions. It only requires to impose a tangential velocity at the boundary while the normal velocity component remains zero. Note that no particle insertions are performed in the above simulations. Nevertheless, these results verify the correctness of the adaptive shear forcing for imposing the proper tangential velocity at the boundary.

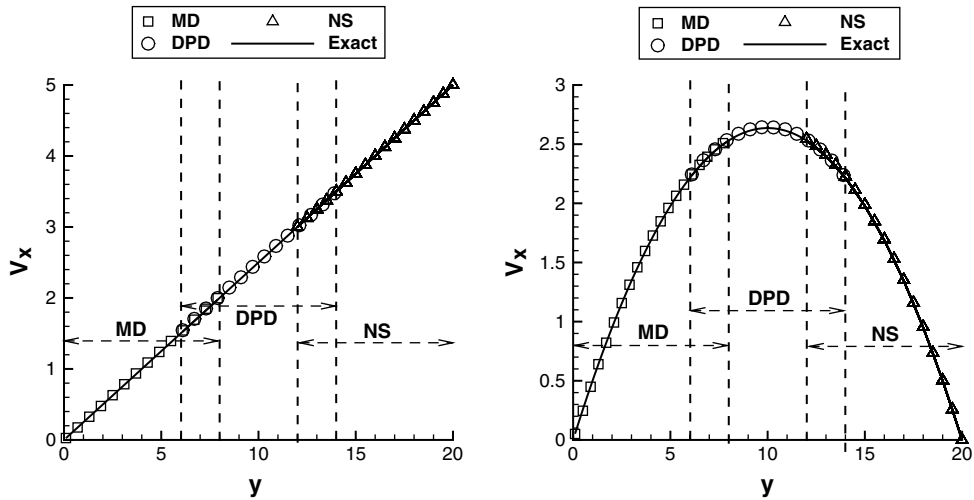


Fig. 3. Couette (left) and Poiseuille (right) flow velocity profiles.

### 3.2. Lid-driven square cavity flow

We selected the well-known lid-driven square cavity flow to test the more general hybrid model system. The Reynolds number of this flow is defined as  $Re = \frac{VL}{\nu}$ , where  $V$  is the velocity of the moving lid and  $L$  is the height of the cavity. Fig. 4 shows a sketch of the simulation domain. The MD and DPD parameters are the same as in Table 1. The MD computational subdomain was set to  $83.3\sigma_{MD} \times 25.0\sigma_{MD} \times 16.7\sigma_{MD}$ , the DPD subdomain to  $50r_c \times 25r_c \times 10r_c$ , and the NS subdomain to  $L \times 0.6L$ , where  $L = 50$  is the characteristic length. In terms of common non-dimensional units the MD subdomain covers the region  $[0, 50] \cap [35, 50]$ , the DPD subdomain is  $[0, 50] \cap [20, 45]$  and the NS subdomain is  $[0, 50] \cap [0, 30]$ , respectively (see Fig. 4). The overlapping regions were set with a thickness of 20% of the characteristic length  $L$ . The MD and DPD regions were assumed to be periodic in the  $z$  direction. The parameters described next are in common non-dimensional units: The kinematic viscosity was 0.576, and the velocity of the moving lid was set to  $V = 0.576$ , which corresponds to  $Re = 50$ . The timestep in the MD and DPD regions was set to 0.005, and in the NS region to 0.015.

Here, the sequence of one iteration was MD  $\rightarrow$  DPD  $\rightarrow$  NS due to the flow propagation from the moving lid to the bottom of the cavity. The inter-region communication was done every time  $\tau = 2.25$ , which corresponds to 450 timesteps in case of the MD and DPD regions, but to 150 timesteps for the NS subdomain. Similarly to the Couette and Poiseuille flow system, we

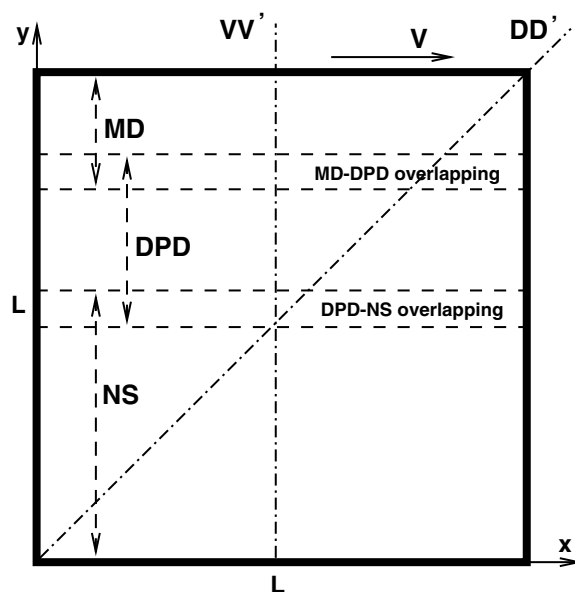


Fig. 4. Lid-driven square cavity flow domain sketch. Comparison of results is performed along the cuts  $VV'$  and  $DD'$ .

estimate here  $M_v = 48.225$  (Eq. (1)) with  $\bar{v} = 0.576$ ,  $E_v = 0.05$  and  $V = 1.66 \times 0.5 \times 10 = 8.33$ , and therefore  $M_v^c = 8680$  (Eq. (2)) with the autocorrelation time  $\tau_v = 0.45$ . Our choice of  $\tau = 2.25$  or 450 timesteps corresponds to the error of approximately 22%, which was done for the purpose of a faster flow convergence to a steady state. However, after steady state was reached, we performed several iterations of the algorithm with each iteration of 9000 timesteps and set the error level below 5% in order to refine the steady state solution. The number of iterations to reach steady state was considerably increased compared to the case of Couette and Poiseuille flows due to the flow complexity and was approximately 500. Also, having the overlapping region thickness less than 10% of the characteristic length yielded a slightly under-developed flow comparable with the flow at a lower Reynolds number (e.g.  $Re = 45$ ). We attribute this to the flow complexity at the interfaces which can be affected by an artificially reduced propagation of the information through a thin overlapping region. In addition, we applied a correction to the boundary velocities extracted from the MD and DPD regions in order to set the total mass flux through the interface to zero (total domain mass conservation). The correction is found to be on the order of several percent of the velocity magnitudes.

Fig. 5 shows hybrid simulation results of the  $Re = 50$  square cavity flow extracted along the  $VV'$  (at the half of the domain) and  $DD'$  lines (see Fig. 4). Results obtained by employing only the full NS equations are plotted with the solid lines, MD results by square symbols, DPD by circles and NS by triangles. The hybrid model solution agrees very well with the highly accurate spectral element solution. Here, velocities at the boundaries contain non-zero tangential as well as normal components. This simulation serves as a rigorous verification of the proposed triple-decker algorithm. In addition, Fig. 6 presents the number density profiles extracted along the  $VV'$  and  $DD'$  lines. The number density in the MD and DPD regions is normalized by the bulk density. In the NS region we assume it to be constant and equal to 1 as we solve the incompressible NS equations.

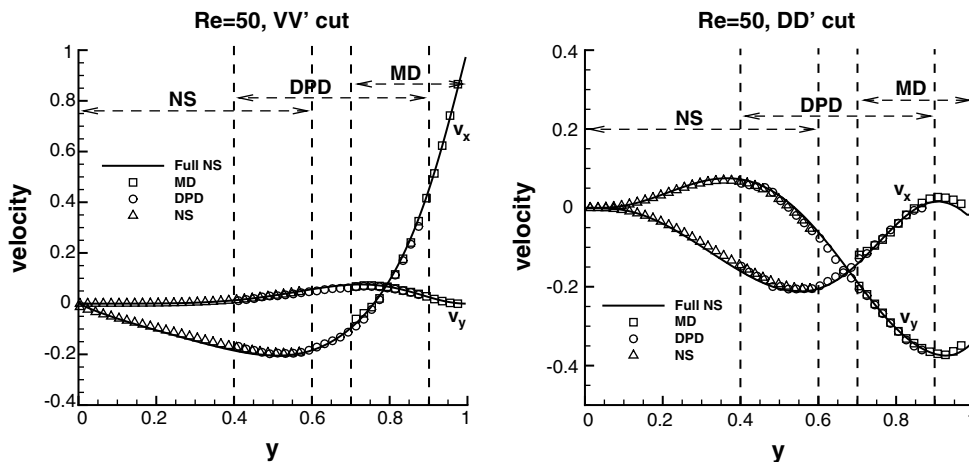


Fig. 5. Velocity profiles extracted along  $VV'$  (left) and  $DD'$  (right) lines. The coordinates and velocities are normalized by the characteristic length and velocity, respectively.  $Re = 50$ .

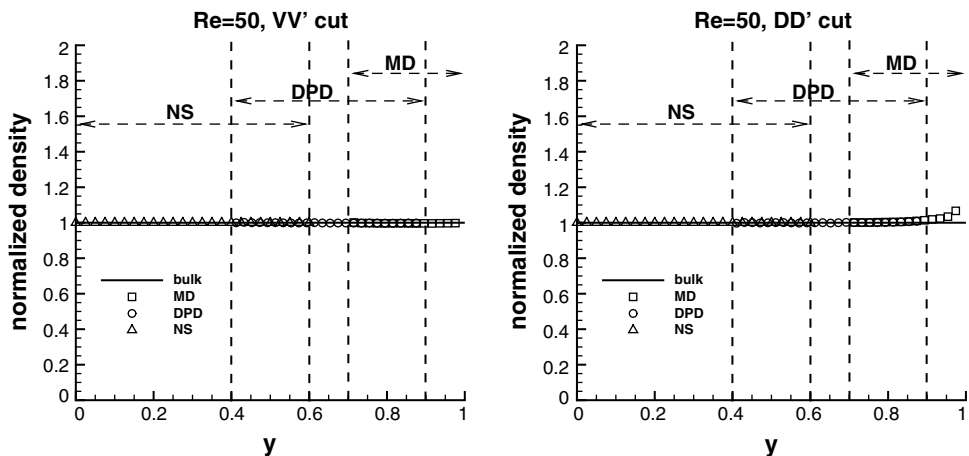


Fig. 6. Number density profiles extracted along  $VV'$  (left) and  $DD'$  (right) lines. The number density is normalized by the bulk density in the case of the MD and DPD regions, and is assumed to be 1 in the NS domain.  $Re = 50$ .

Note that the number density is uniform along the  $VV'$  cut, however we observe a slight density increase in the upper right corner in case of the  $DD'$  cut, where there is particle accumulation in the corner due to the MD fluid being slightly compressible at sufficiently high flow velocity [30]. The influence of the particle accumulation in a wall-bounded geometry on the flow solution was thoroughly studied in the case of the DPD method in [23], where an empirical criterion was established that identifies the maximum allowed flow velocity below which an accurate DPD solution can be obtained. Here, an analogous criterion suggests that the maximum density in the corner normalized by the bulk density should be bounded by 2.0, which corresponds to the maximum lid velocity of approximately 5.0. The values in our simulation are far below the above limits, which justifies why the particle accumulation in the corner has a negligible effect on the flow solution.

Next, we present simulation results of the square cavity flow where the MD, DPD and NS subdomains utilize different non-dimensional characteristic lengths and contain immiscible fluids with different viscosity. However, the Reynolds number of 50 was matched in all regions by scaling the boundary velocities during inter-region communications. For example to scale the velocities for DPD extracted from the MD region, we use the following formula:

$$v_{\text{DPD}}^{\text{BC}} = v_{\text{MD}}^{\text{BC}} \frac{L_{\text{MD}}}{L_{\text{DPD}}} \frac{v_{\text{DPD}}}{v_{\text{MD}}}, \quad (13)$$

where  $L_{\text{MD}}$  and  $L_{\text{DPD}}$  are the characteristic lengths of the MD and DPD regions, and  $v_{\text{MD}}$ ,  $v_{\text{DPD}}$  are the fluid viscosities. Table 2 summarizes the simulation parameters used in the MD and DPD regions. The MD computational subdomain was set to  $100\sigma_{\text{MD}} \times 30\sigma_{\text{MD}} \times 10\sigma_{\text{MD}}$ , the DPD subdomain to  $40r_c \times 20r_c \times 10r_c$  and the NS to  $L \times 0.6L$  with the characteristic lengths  $L_{\text{MD}} = 100\sigma_{\text{MD}}$ ,  $L_{\text{DPD}} = 40r_c$  and  $L_{\text{NS}} = L = 10$ . In non-dimensional units the aforementioned regions correspond to  $100 \times 30 \times 10$  (MD),  $40 \times 20 \times 10$  (DPD) and  $10 \times 6$  (NS), respectively. The simulation domain was similar to that in the Fig. 4 with the overlapping regions having thickness of 20% of the characteristic length, and the MD and DPD regions were set to be periodic in the  $z$  direction. The fluid viscosities were  $v_{\text{MD}} = 2.44$ ,  $v_{\text{DPD}} = 0.54$  and  $v_{\text{NS}} = 0.2$ , and the velocity of the moving lid in the MD subdomain was set to  $V = 1.22$ , which corresponds to  $Re = 50$ . The timestep in the MD and DPD regions was set to 0.00375, and in the NS region to 0.015.

The sequence of one iteration was MD  $\rightarrow$  DPD  $\rightarrow$  NS similar to the previous cavity flow simulation. The inter-region communication was done after the state of the system advances past time  $\tau = 0.75$ , which corresponds to 200 timesteps in case of the MD and DPD regions, but to 50 timesteps for the NS subdomain. Here,  $M_v = 24.28$  (Eq. (1)) with  $\bar{v} = 1.22$ ,  $E_v = 0.05$  and  $V = 3.32 \times 1.0 \times 10 = 33.2$ , and therefore  $M_v^c = 3237$  (Eq. (2)) with the autocorrelation time  $\tau_v = 0.25$ . After steady state was reached with initial inter-communication time  $\tau = 0.75$ , similarly to the previous cavity flow case, in order to refine the steady state solution we performed several iterations with inter-communication time  $\tau = 15$  and set the error below 5%.

Fig. 7 shows hybrid simulation results of the  $Re = 50$  square cavity flow with immiscible fluids extracted along the  $VV'$  and  $DD'$  lines. The hybrid model solution agrees very well with the highly accurate spectral element solution. In addition, Fig. 8 presents the number density profiles extracted along the  $VV'$  and  $DD'$  lines. The number density is nearly constant along the

**Table 2**  
MD and DPD simulation parameters for the cavity flow. Immiscible fluids.

Region	$\epsilon$	$\sigma_{\text{MD}}$	$a$	$n$	$r_c$	$\gamma$	$\sigma$	$k_B T$	$k$ (Eq. (11))
MD	1.0	1.0	N/A	0.6	2.94	2.5	3	1.8	1.0
DPD	N/A	N/A	25	3	1	4.5	3	1	0.25

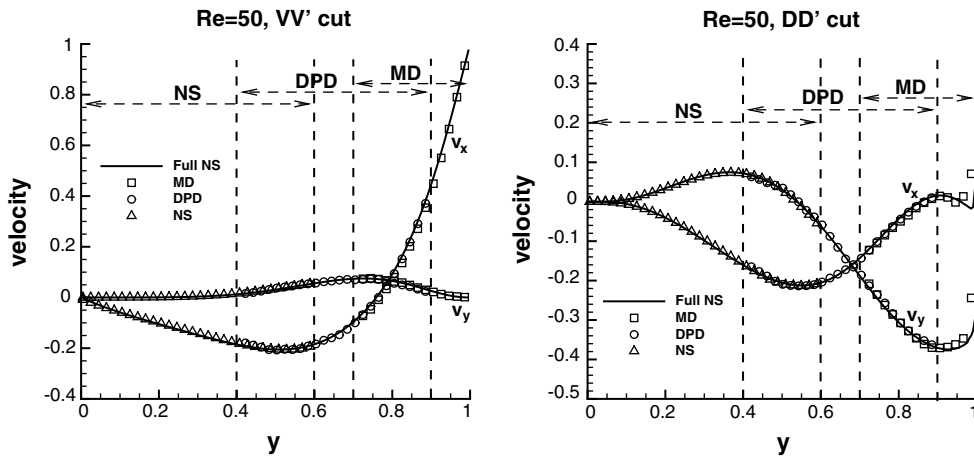


**Fig. 7.** Velocity profiles extracted along  $VV'$  (left) and  $DD'$  (right) lines. The coordinates and velocities are normalized by the characteristic length and velocity, respectively.  $Re = 50$ . Immiscible fluids.

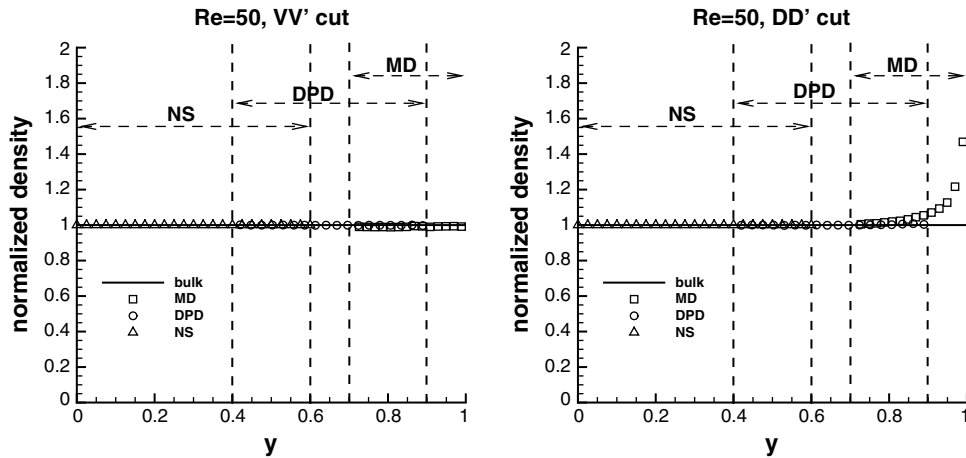


**Fig. 8.** Number density profiles extracted along  $VV'$  (left) and  $DD'$  (right) lines. The number density is normalized by the bulk density in case of the MD and DPD regions, and is assumed to be 1 in the NS domain.  $Re = 50$ . Immiscible fluids.

$VV'$  cut, however we observe a density increase in the corner in case of the  $DD'$  cut. The MD fluid is slightly compressible which permits the particle accumulation in the corner. Here, the normalized density in the corner is higher compared to the cavity flow described above due to a higher velocity of the moving lid. To illustrate the density increase in the corner we provide a normalized density contour plot in Fig. 9. Using our empirical criterion [23] we estimate that the maximum allowed flow velocity below which an accurate solution can be obtained is 6 or the maximum density in the corner is 2.5. Our values are within the stated limits, and therefore particle accumulation in the corner has a negligible effect on the flow solution.

Next, we present an additional cavity test that employs only DPD and NS regions; Fig. 10 shows the domain sketch. We place the DPD subdomain in the right upper corner where we have discontinuous velocity at the boundary. The cavity corner singularity was studied systematically in [31–33] for the case of MD and NS methods. In general, the NS numerical solution in the small neighborhood of such singularity is erroneous and it often gives rise to numerical instability [34]. However, the DPD method does not have such a problem. Note that the left upper corner could be done analogously.

Here the DPD region covers the area of  $\{35 \leq x \leq 50\} \cap \{35 \leq y \leq 50\}$  in the right upper corner of the cavity. The NS region is  $50 \times 50$  excluding the  $\{40 \leq x \leq 50\} \cap \{40 \leq y \leq 50\}$  subregion. The overlapping region thickness is equal to 5, which corresponds to the aforementioned 10% of the characteristic length  $L = 50$ . The DPD parameters used in this simulation were the same as outlined in Table 2. The kinematic viscosity for both descriptions was  $\nu = 0.54$  and the timestep was set to 0.01 in non-dimensional units. The inter-region communication was carried out every  $\tau = 1.0$ . Fig. 11 shows velocity profiles extracted along the  $VV'$  ( $x = 42.5$ ) and  $DD'$  lines for the flow at  $Re = 100$ . Results obtained by the full NS description are plot-

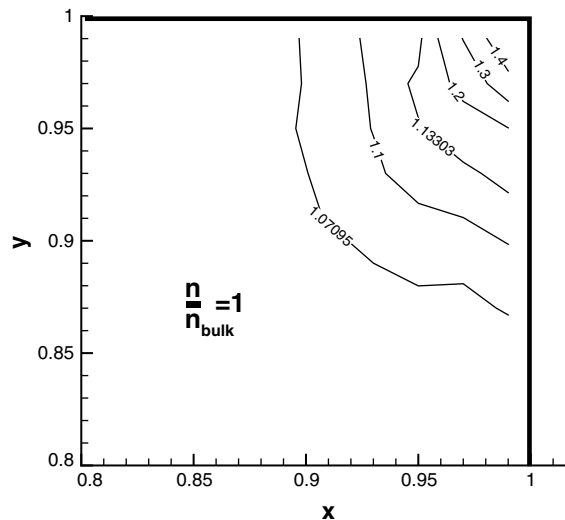


**Fig. 9.** Contour plot of normalized density in the corner. Immiscible fluids.

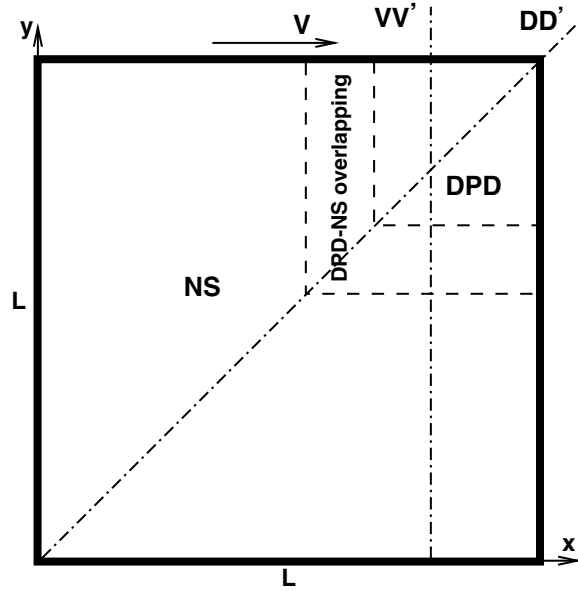


Fig. 10. Lid-driven square cavity flow domain sketch. NS–DPD coupling. Comparison of results is performed along the cuts  $VV'$  and  $DD'$ .

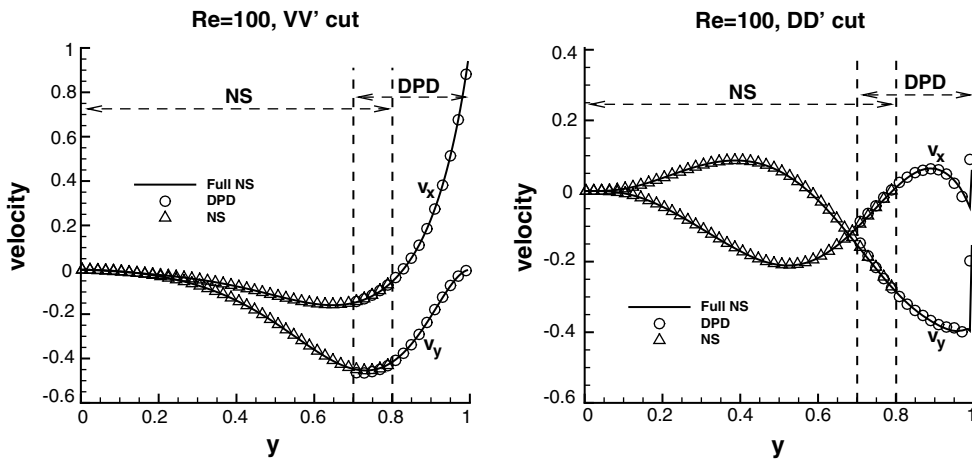


Fig. 11. Velocity profiles extracted along  $VV'$  (left) and  $DD'$  (right) lines. The coordinates and velocities are normalized by the characteristic length and velocity, respectively.  $Re = 100$ .

ted with solid lines, DPD results with circles and NS with triangles. We find an excellent agreement of the hybrid model results with the highly accurate full NS simulation results. Fig. 12 presents the number density profiles extracted along the  $VV'$  and  $DD'$  lines. The number density in the DPD region is normalized by the bulk density, and in the NS region is assumed to be 1. The number density in the domain is nearly uniform, and has only a small deviation in the corner due to the reasons mentioned before. Finally, to illustrate that in the case of the full NS simulation the incompressibility constraint is not satisfied in the small neighborhood of velocity discontinuity point (in the corner) we calculate the divergence of the velocity field. Fig. 13 presents the divergence of velocity extracted along the  $DD'$  line. Nevertheless, we find that for the DPD case the mass in the corner is nearly conserved. The slightly non-zero value of the divergence of velocity is probably due to the particle accumulation effect in the corner described in detail in [23].

### 3.3. Zero overlapping thickness

The triple-decker algorithm presented above requires a non-zero overlapping thickness of the subdomains with different formulations. However, a slight modification of the algorithm enables us to employ zero overlapping thickness, which can be thought of as an interface. Fig. 14 shows the Couette flow domain (left) and the time progression (right) sketch with zero

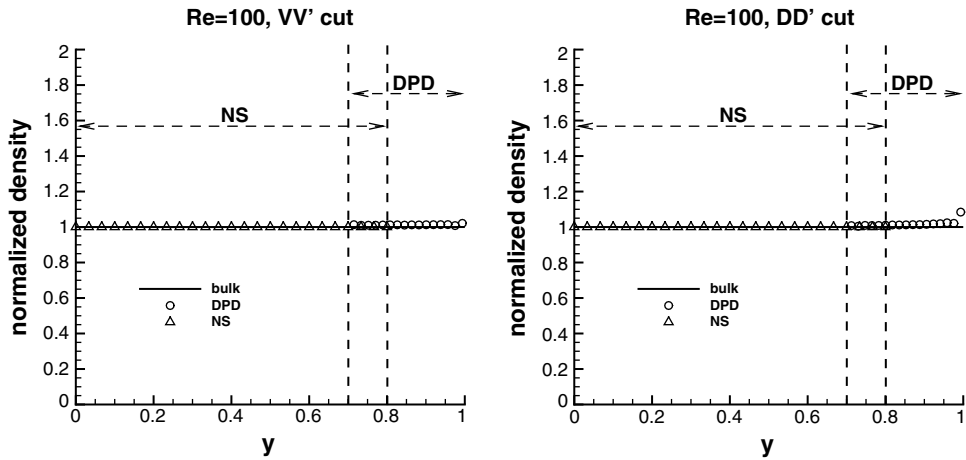


Fig. 12. Number density profiles extracted along VV' (left) and DD' (right) lines. The number density is normalized by the bulk density in case of the DPD region, and is assumed to be 1 in the NS domain.  $Re = 100$ .

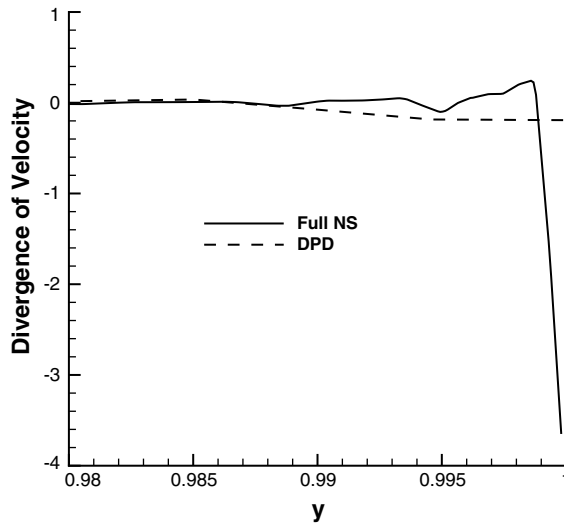


Fig. 13.  $\nabla \cdot \mathbf{v}$  extracted along DD' line for the cases of full NS and DPD.  $Re = 100$ .

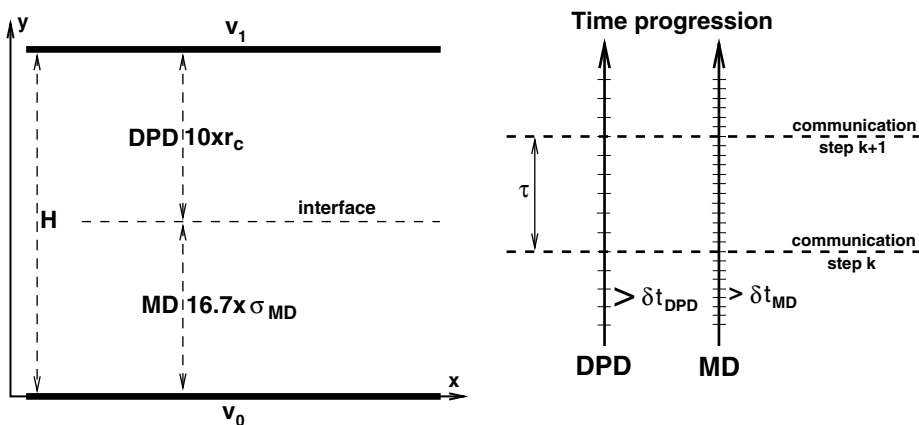


Fig. 14. Couette flow domain (left) and the time progression (right) sketch. Zero overlapping thickness.

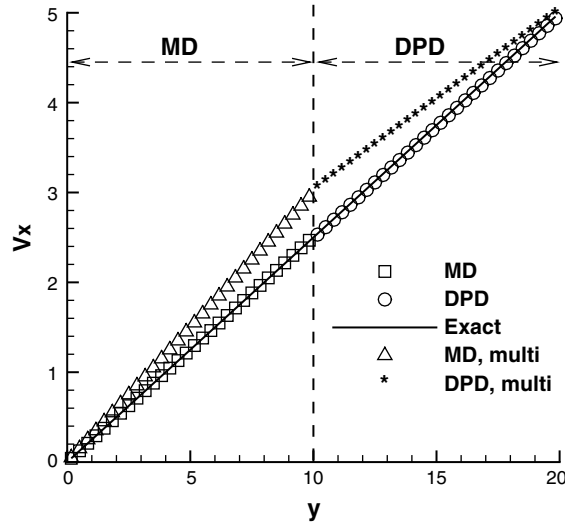


Fig. 15. Couette flow velocity profiles. Zero overlapping thickness.

overlapping thickness. The two walls are placed at  $y = 0$  and  $y = H = 20$  with velocities  $v_0 = 0$  and  $v_1 = 5$ , respectively. The lower half of the domain contains MD fluid and the upper half DPD fluid, and corresponding parameters are described in Table 1. The domain is assumed to be periodic in the  $x$  and  $z$  directions. The boundary conditions at the walls are enforced similarly through the aforementioned adaptive shear force, the pressure force and the specular reflection. However, at the interface we employ the adaptive shear forcing, the definition of which is modified in order to enforce continuous velocity across the interface. Hence,  $\Delta v_t$  in Eq. (5) is defined as  $\Delta v_t = v_t^{\text{MD}} - v_t^{\text{DPD}}$ , where  $v_t^{\text{MD}}$  and  $v_t^{\text{DPD}}$  are the estimated flow velocities at the interface from the MD and DPD regions, respectively. The same iterative procedure (Eq. (5)) is performed until  $\Delta v_t$  converges to zero, which leads to the continuous velocity across the interface. The adaptive shear force  $F_t^k(h)$  is applied in both regions near the interface in counter directions (for instance, positive  $x$  direction in the MD near-interface layer and negative  $x$  direction in the DPD region).

Fig. 15 presents simulation results of Couette flow for the case of zero overlapping thickness. We find an excellent agreement of the results (MD is represented by squares and DPD by circles) with the exact solution (solid line). In this case, the MD and DPD fluids have the same viscosity, and therefore yield the expected linear velocity profile across the channel. In Fig. 15 we also plot Couette flow results with the MD fluid (triangles) having a lower viscosity compared to that of the DPD fluid (stars), which approximates Couette flow for immiscible fluid layers. This test verifies that the adaptive shear force leads to the continuous velocity and shear stress across the interface. In addition, we have observed a uniform density across the channel.

Having zero overlapping thickness among the subdomains is computationally more advantageous compared to the system having non-zero overlaps. However, the example shown above corresponds to zero velocity flux through the MD–DPD interface, and it is not yet clear how to properly impose non-zero normal velocity at the interface in case of arbitrary flow. To this end, the algorithm with zero overlapping thickness is limited at present to simple flows having an interface along the streamlines.

#### 4. Summary

In this paper we have presented a hybrid multiscale method, which is able to cover a broad range of spatiotemporal scales starting from molecular to mesoscopic and to continuum. The molecular region employs the MD method, the mesoscopic utilizes the DPD method, and the continuum is described by the incompressible NS equations.

The scheme is based on the domain decomposition used in the Schwarz alternating method. The corresponding subdomains communicate by passing velocity boundary conditions, which are extracted from one region and subsequently imposed in a receiving region. The choice of a communication pattern among regions with different formulations can be set by a user depending on geometry and flow type. In order to extract flowfield information from particle-based formulations we need to perform averaging during a number of timesteps, which can be varied depending on the characteristic flow velocity and temperature. Imposition of non-periodic boundary conditions involves particle insertion and deletion, specular wall reflection and body force terms. Particles are inserted according to the USHER algorithm in MD region and randomly in near-boundary layer in DPD region. The number of inserted particles is equal to the number of deleted particles in order to ensure mass conservation. The velocities are drawn from an equilibrium Maxwellian distribution. Body forcing includes a boundary pressure force in order to minimize near-boundary density fluctuations, and an adaptive shear force which enforces the tangential velocity component of boundary conditions.

The algorithm is verified for the Couette, Poiseuille and lid-driven cavity flow simulations. The results show very good agreement with analytic and reference solutions. In addition, we showed that the hybrid algorithm can be applied in singularity regions for the NS formulation such as corners in the lid-driven square cavity. Moreover, we presented a spatiotemporal decoupling by utilizing different region dimensions and timesteps in simulations. Finally, we discussed a minimal modification of the algorithm which allowed us to have zero overlapping thickness among the regions with different formulations.

Even though the simulation results presented in this paper were done for two-dimensional flows, we do not see any restrictions to extend the hybrid algorithm to three-dimensional flow cases. Furthermore, future work should consider an extension of algorithm to more complex fluids such as polymeric and biological fluids and suspensions. This type of problems might require more sophisticated particle insertion and body forcing algorithms and potentially the inclusion of additional intra- and inter-molecular, electrostatic and excluded volume interactions. In addition, such systems might need an inter-exchange with more detailed information, for instance polymeric stresses. In turn, in the continuum region the incompressible NS equations might need to be substituted by more appropriate visco-elastic continuum non-Newtonian fluid models.

## Acknowledgment

This work was supported by NSF grants IMAG and CI-TEAM. Simulations were run on the SDSC IBM Blue Gene computer.

## References

- [1] G.E. Karniadakis, A. Beskok, N.R. Aluru, *Microflows and Nanoflows: Fundamentals and Simulation*, Springer, New York, 2005.
- [2] M. Antia, T. Herricks, P.K. Rathod, Microfluidic modeling of cell–cell interactions in malaria pathogenesis, *PLoS Pathogens* 3 (7) (2007) 939–945.
- [3] I.V. Pivkin, P.D. Richardson, G.E. Karniadakis, Blood flow velocity effects and role of activation delay time on growth and form of platelet thrombi, *Proceedings of the National Academy of Sciences USA* 103 (46) (2006) 17164–17169.
- [4] S.T. O’Connell, P.A. Thompson, Molecular dynamics–continuum hybrid computations: a tool for studying complex fluid flows, *Physical Review E* 52 (6) (1995) 5792–5795.
- [5] E.G. Flekkoy, G. Wagner, J. Feder, Hybrid model for combined particle and continuum dynamics, *Europhysics Letters* 52 (3) (2000) 271–276.
- [6] X.B. Nie, S.Y. Chen, W.N. E, M.O. Robbins, A continuum and molecular dynamics hybrid method for micro- and nano-fluid flow, *Journal of Fluid Mechanics* 500 (2004) 55–64.
- [7] R. Delgado-Buscalioni, P.V. Coveney, Continuum–particle hybrid coupling for mass, momentum, and energy transfers in unsteady fluid flow, *Physical Review E* 67 (4) (2003) 046704.
- [8] N.G. Hadjiconstantinou, Hybrid atomistic–continuum formulations and the moving contact-line problem, *Journal of Computational Physics* 154 (2) (1999) 245–265.
- [9] T. Werder, J.H. Walther, P. Koumoutsakos, Hybrid atomistic–continuum method for the simulation of dense fluid flows, *Journal of Computational Physics* 205 (1) (2005) 373–390.
- [10] Y.C. Wang, G.W. He, A dynamic coupling model for hybrid atomistic–continuum computations, *Chemical Engineering Science* 62 (2007) 3574–3579.
- [11] S. Succi, *The Lattice Boltzmann Equation for Fluid Dynamics and Beyond*, Oxford University Press, Oxford, 2001.
- [12] P.J. Hoogerbrugge, J.M.V.A. Koelman, Simulating microscopic hydrodynamic phenomena with dissipative particle dynamics, *Europhysics Letters* 19 (3) (1992) 155–160.
- [13] R.D. Groot, P.B. Warren, Dissipative particle dynamics: bridging the gap between atomistic and mesoscopic simulation, *Journal of Chemical Physics* 107 (11) (1997) 4423–4435.
- [14] A. Tartakovsky, P. Meakin, T.D. Scheibe, R.E. West, Simulations of reactive transport and precipitation with smoothed particle hydrodynamics, *Journal of Computational Physics* 222 (2007) 654–672.
- [15] R. Ata, A. Soulaïmani, A stabilized SPH method for inviscid shallow water flows, *International Journal for Numerical Methods in Fluids* 47 (2) (2005) 139–159.
- [16] M. Fyta, S. Melchionna, E. Kaxiras, S. Succi, Coupling Lattice Boltzmann with atomistic dynamics for the multiscale simulation of nano-biological flows, *Computing in Science and Engineering*, arXiv:0710.1272v1.
- [17] A. Dupuis, E.M. Kotsalis, P. Koumoutsakos, Coupling Lattice Boltzmann and molecular dynamics models for dense fluids, *Physical Review E* 75 (4) (2007) 046704.
- [18] B.F. Smith, P.E. Bjorstad, W.D. Gropp, *Domain Decomposition: Parallel Multilevel Methods for Elliptic Partial Differential equations*, Cambridge University Press, Cambridge, 1996.
- [19] N.G. Hadjiconstantinou, A.L. Garcia, M.Z. Bazant, G. He, Statistical error in particle simulations of hydrodynamic phenomena, *Journal of Computational Physics* 187 (1) (2003) 274–297.
- [20] W. Janke, Statistical analysis of simulations: data correlations and error estimation, in: *Proceedings of the Euro Winter School Quantum Simulations of Complex Many-Body Systems: From Theory to Algorithms*, John von Neumann Institute for Computing (NIC), vol. 10, 2002, pp. 423–445.
- [21] T. Soddemann, B. Duenweg, K. Kremer, Dissipative particle dynamics: a useful thermostat for equilibrium and nonequilibrium molecular dynamics simulations, *Physical Review E* 68 (4) (2003) 046702.
- [22] R. Delgado-Buscalioni, P.V. Coveney, USHER: an algorithm for particle insertion in dense fluids, *Journal of Chemical Physics* 119 (2) (2003) 978–987.
- [23] D.A. Fedosov, I.V. Pivkin, G.E. Karniadakis, Velocity limit in DPD simulations of wall-bounded flows, *Journal of Computational Physics* 227 (4) (2008) 2540–2559.
- [24] P. Espanol, P. Warren, Statistical mechanics of dissipative particle dynamics, *Europhysics Letters* 30 (4) (1995) 191–196.
- [25] X. Fan, N. Phan-Thien, S. Chen, X. Wu, T.Y. Ng, Simulating flow of DNA suspension using dissipative particle dynamics, *Physics of Fluids* 18 (6) (2006) 063102.
- [26] V. Symeonidis, B. Caswell, G.E. Karniadakis, Schmidt number effects in dissipative particle dynamics simulation of polymers, *Journal of Chemical Physics* 125 (2006) 184902.
- [27] I.V. Pivkin, G.E. Karniadakis, Controlling density fluctuations in wall-bounded DPD systems, *Physical Review Letters* 96 (2006) 206001.
- [28] G.E. Karniadakis, S.J. Sherwin, *Spectral/hp Element Methods for CFD*, Oxford University Press, Oxford, 2005.
- [29] J.A. Backer, C.P. Lowe, H.C.J. Hoefsloot, P.D. Ledema, Poiseuille flow to measure the viscosity of particle model fluids, *Journal of Chemical Physics* 122 (2005) 154503.
- [30] M. Sun, C. Ebner, Molecular-dynamics simulation of compressible fluid flow in two-dimensional channels, *Physical Review A* 48 (8) (1992) 4813–4818.

- [31] J. Koplik, J.R. Banavar, Corner flow in the sliding plate problem, *Physics of Fluids* 7 (12) (1995) 3118.
- [32] X. Nie, S. Chen, M.O. Robbins, Hybrid continuum–atomistic simulation of singular corner flow, *Physics of Fluids* 16 (10) (2004) 3579.
- [33] X. Nie, M.O. Robbins, S. Chen, Resolving singular forces in cavity flow: multiscale modeling from atomic to millimeter scales, *Physical Review Letters* 96 (2006) 134501.
- [34] W.W. Schultz, N.Y. Lee, J.P. Boyd, Chebyshev pseudospectral method of viscous flows with corner singularities, *Journal of Scientific Computing* 4 (1) (1989) 1–24.